



**HAL**  
open science

## Directional Crystallization from the Melt of an Organic p-Type and n-Type Semiconductor Blend

Guangfeng Liu, Jie Liu, Andrew Dunn, Peter Nadazdy, Peter Siffalovic,  
Roland Resel, Mamatimin Abbas, Guillaume Wantz, Yves Henri Geerts

► **To cite this version:**

Guangfeng Liu, Jie Liu, Andrew Dunn, Peter Nadazdy, Peter Siffalovic, et al.. Directional Crystallization from the Melt of an Organic p-Type and n-Type Semiconductor Blend. *Crystal Growth & Design*, 2021, 21 (9), pp.5231-5239. 10.1021/acs.cgd.1c00570 . hal-03434758

**HAL Id: hal-03434758**

**<https://hal.science/hal-03434758>**

Submitted on 23 Nov 2021

**HAL** is a multi-disciplinary open access archive for the deposit and dissemination of scientific research documents, whether they are published or not. The documents may come from teaching and research institutions in France or abroad, or from public or private research centers.

L'archive ouverte pluridisciplinaire **HAL**, est destinée au dépôt et à la diffusion de documents scientifiques de niveau recherche, publiés ou non, émanant des établissements d'enseignement et de recherche français ou étrangers, des laboratoires publics ou privés.

# Directional crystallization from melt of an organic p-type & n-type semiconductor blend

*Guangfeng Liu,<sup>1\*</sup> Jie Liu<sup>1</sup>, Andrew S. Dunn<sup>1</sup>, Peter Nadazdy<sup>3</sup>, Peter Siffalovic<sup>3,6</sup>, Roland Resel<sup>2</sup> Mamatimin Abbas<sup>4</sup>, Guillaume Wantz<sup>4</sup> and Yves Henri Geerts<sup>1,5</sup>*

- 1) Laboratoire de chimie des polymères, Faculté des Sciences, Université Libre de Bruxelles (ULB), CP 206/01, Boulevard du Triomphe, 1050, Brussels, Belgium
- 2) Institute of Solid State Physics, Graz University of Technology, Petersgasse 16, 8010 Graz, Austria.
- 3) Institute of Physics, Slovak Academy of Sciences, Dubravska cesta 9, 84511 Bratislava, Slovakia.
- 4) Université de Bordeaux, IMS, CNRS, UMR-5218, Bordeaux INP, ENSCBP, 33405 Talence, France
- 5) International Solvay Institutes of Physics and Chemistry, ULB, CP 231, Boulevard du Triomphe, 1050 Brussels, Belgium
- 6) Centre for Advanced Materials Application, Dubravska cesta 9, 84511 Bratislava, Slovakia

## ABSTRACT

Directional crystallization from the melt has been used as a tool to grow parallel crystalline stripes of p- and n-type molecular semiconductors. To start, the phase behavior of 2,7-dioctyl[1]benzothieno[3,2-*b*][1]benzothiophene (C8-BTBT-C8): tetracyanoquinodimethane (TCNQ) blends (molar ratio from 20:1 to 1:1) has been investigated by variable temperature X-ray diffraction, differential scanning calorimetry, and polarized optical microscopy. The partial charge transfer between C8-BTBT-C8 donor and TCNQ acceptor as a function of temperature have been studied. Blends of 10:1 and 20:1 have been selected for directional crystallization because they show similar thermotropic and phase behavior comparable to pure C8-BTBT-C8. Directional crystallization results suggest that moderate cooling rates (6 and 12 °C min<sup>-1</sup>) leads to a digitated growth mode that gives rise to parallel crystalline stripes of C8-BTBT-C8 and C8-BTBT-C8-TCNQ charge transfer complexes (C8-BTBT-C8-TCNQ CT), as confirmed by confocal Raman imaging. X-ray diffraction reveals high preferential orientation and good in-plane alignment for both C8-BTBT-C8 and C8-BTBT-C8-TCNQ CT crystallites.

## INTRODUCTION

Pristine organic semiconductors possess a low electrical conductivity, and usually, their dielectric constant is in the order of 3-4. However, a new situation occurs when they are doped, as shown by Heeger, McDiarmid, and Shirakawa in 1977.<sup>1</sup> Doping, which consists of the external introduction of charges into semiconductors with chemicals, electric field, or light, gives rise to an increase of electrical conductivity, up to 11 orders of magnitude in the case of polyacetylene.<sup>2</sup> Doped organic semiconductors have been the topic of intense research activities for more than four decades.<sup>3-5</sup> However, some fundamental questions remain unanswered, even today. Why, for example, the ratio of free charge carriers to the number of dopant molecules,  $\eta_{dop}$ , is so low, reaching only an order of magnitude of 10% in most systems? This might be caused by the low dielectric constant of organic semiconductors that opposes charge separation, the clustering of dopant molecules, the trapping of charge carriers, or a strong hybridization of dopant and matrix molecules.<sup>4,5</sup> While relatively uniform dispersion and distribution of dopants can be achieved in conjugated polymers, the situation is more complicated for small molecular semiconductors, especially when they crystallize. The dispersion and distribution of doping agents depend on various factors, such as: i) the crystal lattice of the host semiconductor and the size of the guest atoms or molecules, ii) the stoichiometry, iii) the crystallization conditions, iv) the occurrence of structural defects, v) the presence of grain boundaries and vi) the miscibility and extent of charge transfer between donors and acceptors.<sup>6</sup> So far, only a few doped single crystals of molecular semiconductors have been reported. For example, Hiramoto et al. have reported single crystals of rubrene doped with minute amounts of iron(III) chloride.<sup>7</sup>

In a different field of research, the directional crystallization of thin films of organic molecules in the presence of a deliberately introduced impurities of various amounts has been extensively

studied for the occurrence of Mullins-Sekerka instabilities and pattern formation at the growth front.<sup>8-12</sup> Typically, eutectic mixtures forming one miscible phase in melt and two separate crystal phases have been subjected to directional crystallization in a temperature gradient,  $\nabla T$ , using an experimental set-up as described in Figure 1.<sup>13</sup> At the growth front, the interface between the liquid and solid phases, crystal growth and diffusion of the phases compete. The length-scale of phase separation between the two crystal phases is linked to the cooling rate at the growth front,  $C_{\text{front}}$  ( $^{\circ}\text{C min}^{-1}$ ), that is externally imposed by the lateral withdrawal velocity,  $V_p$  ( $\mu\text{m s}^{-1}$ ), and the magnitude of the thermal gradient,  $G_{\text{exp}}$ , ( $^{\circ}\text{C mm}^{-1}$ ). As a function of experimental conditions, digitated, dendritic, or even more complex growth morphologies are essentially observed.<sup>13-15</sup>

In this paper, we combine these two aforementioned seemingly separate research fields to control the morphology of thin films of 2,7-dioctyl[1]benzothieno[3,2-*b*][1]benzothiophene (C8-BTBT-C8) with various amounts of tetracyanoquinodimethane (TCNQ). These two organic semiconductors have been selected because the crystal structure of their charge transfer complexes has already been reported<sup>16,17</sup>(Figure S1 and Table S1), allowing a detailed structural elucidation of thin-film morphology. The latter is defined here as comprising of crystal shape, crystal size, crystal orientation, crystal alignment, less ordered regions, defects, eventual polymorphs, and grain boundaries. Our goal is to obtain parallel crystalline stripes of C8-BTBT-C8 separated by stripes of C8-BTBT-C8-TCNQ charge transfer complexes (C8-BTBT-C8-TCNQ CT).

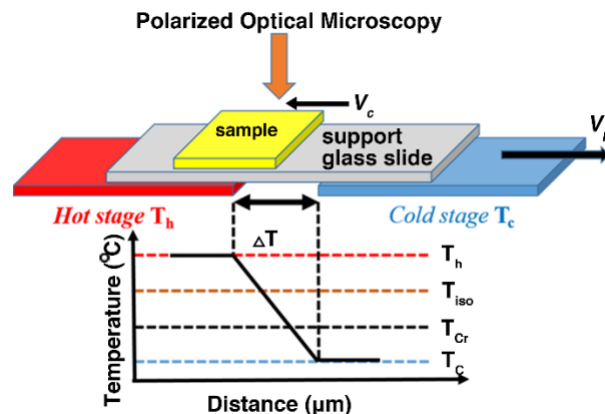


**Figure 1.** Schematic diagram of the  $\nabla T$  set-up.  $T_{\text{iso}}$  and  $T_{\text{Cr}}$  are the isotropic melt and crystallization temperatures, respectively (recorded by DSC).  $T_{\text{h}}$  and  $T_{\text{c}}$  are the temperatures of the hot and cold stages, respectively.  $\Delta T$  is the temperature difference between the hot and cold stages.  $V_{\text{p}}$  and  $V_{\text{c}}$  are the lateral withdrawal velocity and crystal growth rate of the sample, respectively.

## EXPERIMENTAL SECTION

**1. Materials.** C8-BTBT-C8 and 2,7-bis(dodecyloxy)[1]benzothieno[3,2-b]-benzothiophene (C12-BTBT-C12) were synthesized according to literature.<sup>18</sup> Purification of the materials was performed through a chromatographic column using hexane and the purity assessed by NMR.<sup>19</sup> 7,7,8,8-tetracyanoquinodimethane (TCNQ, >98%, Sigma-Aldrich), polydimethylsiloxane (PDMS, trade name: SYLGARD®184, Sigma-Aldrich), and HPLC-grade (>99.8%, Sigma-Aldrich) toluene solvent were used without further purification. Glass substrates of size 15 mm × 15 mm × 0.16 mm (D 263 Borosilicate thin glass from Marienfeld, Germany) were sonicated for 10 minutes in deionized water and acetone, then dried with nitrogen and exposed to an ultraviolet-ozone (Procleaner plus; Bioforce Nanosciences) treatment for 30 minutes before each experiment.

*Glass surface modification by PDMS (SYLGARD®184)*: PDMS was mixed with a curing agent in a 10:1 w/w ratio. Then, this solution was diluted in toluene in a 1:4 (w/w) ratio. Next, the diluted PDMS solution was spin-coated onto the pre-cleaned 15 mm × 15 mm × 0.16 mm glass substrates at a speed of 6000 rpm. Finally, glass substrates coated with PDMS were heated for 2 hours at 90°C for completely curing. The thickness of the PDMS layer, measured by an Alpha-Step D-600 Stylus Profiler, KLA-Tencor, was found to be ~ 350 nm. The surface roughness (Ra) of the layer, measured using a Veeco NT9080 optical profilometer, was around 7 nm. For the preparation of powder blended samples, C8-BTBT-C8 and TCNQ were mixed in molar ratios 1:1, 10:1 and 20:1. Then, each blend was ground with a mortar and pestle for 10 min at room temperature in order to disperse TCNQ molecules in the rich phase of C8-BTBT-C8. For the preparation of thin films, 0.5 mg of C8-BTBT-C8:TCNQ blended powder (either 10:1 or 20:1) was deposited on a 15 mm × 15 mm × 0.16 mm pre-cleaned thin glass substrate (or a PDMS/glass substrate) and covered by another identical glass substrate (or a PDMS/glass substrate). Then, the whole sample was placed on the hot stage at 130°C in order to obtain a uniform liquid crystal phase. Each thin film was then produced by processing the sample by directional crystallization. After the treatment, the cover substrate was removed for X-ray diffraction analysis. For the thin films prepared on pure glass substrates, removing the cover glass resulted in almost equal amounts of material on both glass slides (both still usable for X-ray diffraction measurements). However, for the thin films prepared on PDMS/glass substrates, removing the cover PDMS/glass led most of the material on the bottom PDMS/glass substrate.

**2. Temperature gradient apparatus.** The set-up shown in Figure 1, consists of a *Linkam GS350* system presenting two distinct heating stages separated by a gap. The distance (gap) between the two stages where the thermal gradient was generated was 2 mm. A 76 mm × 26 mm × 1 mm

microscope glass slide (Marienfeld Cat. No. 1000000) was intercalated between the stages and the sample to ensure a constant displacement velocity of the sample. During the  $\nabla T$  experiments, the hot stage was set at a temperature  $T_h = 130^\circ\text{C}$ ; while the cold stage was maintained at a temperature  $T_c = 80^\circ\text{C}$ . The system is covered by a hermetic lid so that the system is thermally independent of the laboratory environment.

**3. Calibration of the magnitude of the temperature gradient set-up ( $G_{cal}$ ).** Previous work<sup>20</sup> has shown that the effective magnitude of the temperature gradient ( $G_{exp}$ ) that takes place between the hot and cold zones is less than the magnitude calculated by the equation as  $G = (T_h - T_c)/x$ , where  $x = 2.0$  mm (the gap between the hot and cold stages). The calibration of the  $\nabla T$  set-up has been carried out as previously reported and is detailed in supporting information (Table S2 and Figure S2).  $G_{exp} \approx 10^\circ\text{C mm}^{-1}$  for the  $T_h - T_c$  couple as  $130^\circ\text{C} - 80^\circ\text{C}$ .

**4. Thermogravimetric analysis (TGA).** TGA measurements were performed with a Perkin Elmer Pyris 6 TGA instrument. The powder samples of pure C8-BTBT-C8, C8-BTBT-C8:TCNQ blends and pure TCNQ underwent a linear ramp of increasing temperature up to  $500^\circ\text{C}$  at a rate of  $30^\circ\text{C min}^{-1}$  in an inert atmosphere of nitrogen. Moreover, to further test the thermal stability, the C8-BTBT-C8:TCNQ blended powder samples were also heated to  $160^\circ\text{C}$  and  $200^\circ\text{C}$  and maintained under flowing nitrogen gas for 1 hour.

**5. Differential scanning calorimetry (DSC).** DSC measurements were performed for pure C8-BTBT-C8 powder, C8-BTBT-C8:TCNQ blended powders and pure TCNQ under a dry nitrogen gas atmosphere in a NETZSCH POLYMA DSC 214 instrument (temperature range  $25^\circ\text{C} - 160^\circ\text{C}$ ). First, each sample was measured using  $10^\circ\text{C min}^{-1}$  heating-cooling rates with three heating-cooling cycles. Then, to investigate the effect of heating and cooling rate on DSC peak shapes, a heating-

cooling rate of  $1^{\circ}\text{C min}^{-1}$  with three heating-cooling cycles was adopted for each sample. The data were analyzed using the software *Netzsch Proteus version 7.1*.<sup>21</sup>

**6. Polarized Optical Microscopy (POM).** The liquid crystals and crystallization behaviors of the powder samples of pure C8-BTBT-C8, C8-BTBT-C8:TCNQ blends were recorded at different temperatures by a hot-stage-POM (*Linkam LTS350-Nikon Eclipse 80i*). Another hot-stage-POM (*Linkam GS350-Nikon Eclipse 80i*) allowed *in situ* observations of the temperature gradient crystallization of the thin films. Images of the thin film samples were recorded during and after the thermal gradient treatments.

**7. Crystal morphology calculation.** The crystal morphology of C8-BTBT-C8 and C8-BTBT-C8:TCNQ CT was modeled from the crystal structure obtained from Cambridge Structural Database (CSD) with codes YOKBIK<sup>18</sup> and WOTWUZ,<sup>17</sup> respectively, using Mercury 3.10.3 software based on the Bravais-Friedel-Donnay-Harker (BFDH) method.<sup>22-24</sup>

## **8. X-ray measurements.**

**Specular X-ray diffraction (sXRD):** sXRD patterns of the thin films were collected on a Bruker D8 Advance diffractometer using Cu K $\alpha$  radiation ( $\lambda = 1.5418 \text{ \AA}$ ). Measurements were conducted at room temperature in the  $2\theta$  range between  $1.6^{\circ}$  and  $30^{\circ}$  with an increment of  $0.02^{\circ}$  per step and a counting time of 3s per step. XRD curves are plotted as the scattering intensity versus the scattering wave vector,  $q_z$  ( $\text{\AA}^{-1}$ ), using the equation  $q = 4\pi \times \sin\theta/\lambda$ , where  $\lambda = 1.5418 \text{ \AA}$ . Powder XRD patterns (PXRD) for the powder samples of pure C8-BTBT-C8 and C8-BTBT-C8: TCNQ blends were collected on a Rigaku Ultima IV diffractometer using Cu K $\alpha$  radiation. Measurements were conducted at room temperature in the  $2\theta$  range between  $1.6^{\circ}$  and  $50^{\circ}$  with an increment of  $0.02^{\circ}$  per step and a counting time of 0.24 s per step. The variable temperature PXRD patterns of

the samples were recorded using a DHS 1100 (Anton Paar company) heating stage on the Rigaku instrument, with the same scan parameters and 10 °C min<sup>-1</sup> heating-cooling rates.

**Grazing-incidence X-ray diffraction (GIXD):** GIXD experiments for thin films were carried out on the XRD1 beamline at the Elettra synchrotron (Trieste), using standard set-up. The X-ray wavelength in these experiments was 1.4 Å. The scattered intensities were collected by a two-dimensional X-ray detector (Pilatus 2M, Dectris). Calibration was performed using LaB<sub>6</sub> standard. An incident angle of  $\alpha_i = 3^\circ$  was chosen to reduce the width of the diffraction peaks. During each GIXD experiment, the samples were rotated by 360°, integrating the intensity during a rotation angle of 2°. In total, 180 diffraction patterns were acquired for each sample. Data processing was performed by the software GIDVis<sup>25</sup> for phase analysis and calculation of pole figures. STEREOPOLE<sup>26</sup> software was used for the interpretation of the pole figures.

**9. Confocal Raman microscopy (CRM):** Spatially-resolved Raman spectra were measured by a commercial CRM system (Alpha300 R+, WITec). The excitation laser wavelength was 532 nm. The spectrophotometer (UHTS 300, WITec), equipped with a 600 gr/mm grating (blazed at 500 nm) and coupled to an EMCCD camera (Newton DU970N BV 353, Andor), was employed to collect Raman spectra through a 100 µm diameter multimode optical fiber that also served as a confocal pinhole. The measured spectra were acquired and analyzed using WITec Project Plus software.

## RESULTS AND DISCUSSION

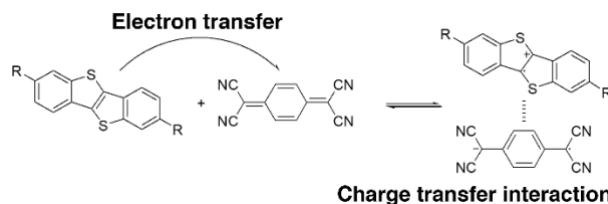
### 1. Preparation and thermotropic behaviors of C8-BTBT-C8: TCNQ blends.

The thermal stability of pure C8-BTBT-C8, TCNQ, and C8-BTBT-C8:TCNQ blends (10:1 and 20:1 molar ratios), up to 200°C, were assessed by TGA; blends of 1:1 tend to be slightly less stable

(see detailed description in the supporting information, Figure S3, S4 and S5). DSC measurements indicate that TCNQ has no transition in the temperature range from 25°C to 160°C (Figure S6), whereas C8-BTBT-C8 exhibits the expected Cr to LC (liquid crystal phase) and LC to isotropic melt phase transitions: at 109.8°C and 126.0°C, respectively (Figure 2a). Variable temperature PXRD and POM results confirm the presence of the known crystal structure of pure C8-BTBT-C8 at room temperature and the smectic-A (SmA) phase at high temperature (see Figure S13a, and S14, see also Table S4). These results agree with previous reports.<sup>18,20</sup>

For investigating the thermotropic phase behaviors of the blends, the starting point is 1:1 ratio of C8-BTBT-C8 and TCNQ. Grinding, which is an incomplete mixing process, affords a coarse blend with grains of C8-BTBT-C8, TCNQ, and C8-BTBT-C8-TCNQ CT, as shown by PXRD (Figure S11). Raising the temperature enhances mixing and allows electron transfer from C8-BTBT-C8 to TCNQ crystals. This is corroborated by the variable temperature PXRD patterns of 1:1 blend (Figure S13b). However, at 160 °C, some Bragg peaks are still observed in the XRD pattern, indicating that the blend does not form an isotropic melt. This is confirmed by the POM image at 160 °C, which shows some texture (Figure S15). The second and the third heating-cooling DSC cycles (10 °C min<sup>-1</sup> and 1 °C min<sup>-1</sup> scanning rates) of 1:1 blend are comparable with one another (Figures S7b and S7c, Figure S8b and S8c). However, the first heating cycle is different because of incomplete mixing by grinding (Figure S7a and Figure S8a). The similarity of the second and third heating curves indicates that C8-BTBT-C8 and C8-BTBT-C8-TCNQ CT have reached phases with equilibrium compositions. This conclusion is also corroborated by the similarity of the relative crystallization enthalpies (Figure S7, S8 and Table S3). These results highlight that a partial electron transfer occurs between C8-BTBT-C8 and TCNQ in 1:1 blend. An

equilibrium takes place as described in Scheme 1, which depends upon temperature but also on the phase behavior.



**Scheme 1.** Partial electron transfer occurring between the donor C8-BTBT-C8 and the acceptor TCNQ (R = C<sub>8</sub>H<sub>17</sub>).

Since the phase behavior of 1:1 blend is particularly complex, we have decided to investigate the thermal behavior of 10:1 and 20:1 blends, expecting that they would deviate less from that of pure C8-BTBT-C8. Figure S12a shows the comparison of the PXRD pattern of the powder sample of pure C8-BTBT-C8, 10:1 and 20:1 blends, after grinding, at room temperature. Only Bragg peaks belonging to the crystal structure of C8-BTBT-C8 crystals can be observed in the PXRD patterns, indicating that TCNQ molecules were molecularly dispersed in the C8-BTBT-C8 rich phase. Notably, C8-BTBT-C8-TCNQ CT co-crystals were not detected in these two blends at room temperature. Figure S12b and Figure 2c show the variable temperature PXRD patterns of 10:1 and 20:1 blends, which exhibit similar phase behavior, *i.e.* at 90°C, C8-BTBT-C8-TCNQ CT co-crystals can be detected. At 130°C, the blends transform into a SmA liquid crystal phase. At 160°C, the isotropic melt formed. Cooled down to room temperature, C8-BTBT-C8 and C8-BTBT-C8-TCNQ CT co-crystals are detected but no TCNQ is observed (see detail description in the supporting information, also see Figure S12b, and Table S4). These diffraction results match the POM observations of the two blends at both 130 °C and 160 °C very well (Figure S16). Comparing the DSC curves of 1:1 blend, 10:1 and 20:1 blends, the DSC traces are much less complex (Figure 2b, Figure S9 and S10). In the first heating cycles of the blends, the LC to the isotropic melt phase

transition temperatures ( $T_{LC-iso}$ ) for 10:1 and 20:1 blends are 135.0°C and 131.6°C, respectively, which are higher than for pure C8-BTBT-C8 (126.0°C). Impurities are known to depress melting points because the chemical potential of a mixture is always lower than that of its individual constituents. However, some electrostatic interactions arise from charge transfer complex formation, which increases  $T_{LC-iso}$ . The second and third heating cycles, as well as the first, second and third cooling cycles, of the blends that are comparable with one another, demonstrate reproducibility and consistency of the system (see detailed description in the supporting information, also see Figure 2b, Figure S9, S10 and Table S3). In conclusion, the above results are consistent with the view that the blends have reached phases with equilibrium compositions after the first heating. Blends of 10:1 and 20:1 exhibit a more simple and comparable phase behavior to pure C8-BTBT-C8, meaning they qualify as good candidates for directional crystallization.

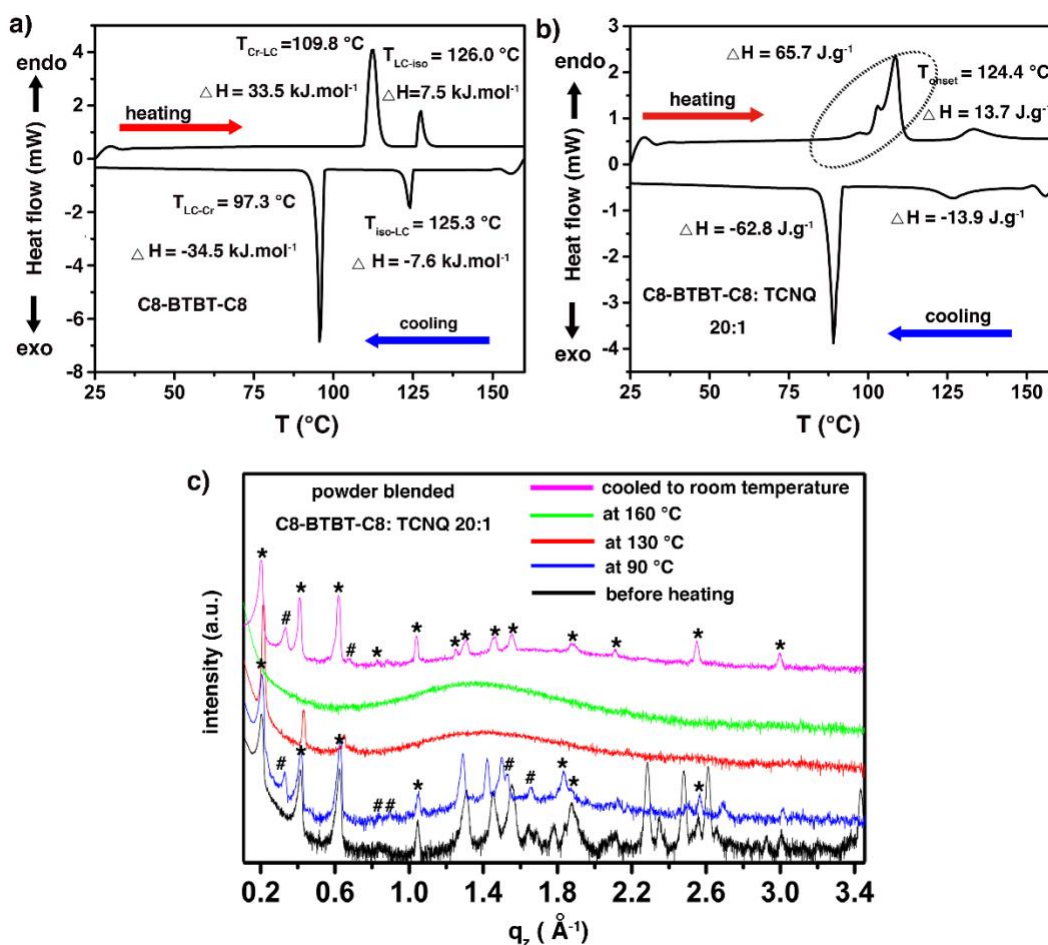


**Figure 2.** DSC traces of (a) pure C8-BTBT-C8 and (b) C8-BTBT-C8:TCNQ blend with molar ratio 20:1. The DSC traces shown here are the second heating-cooling cycle of pure C8-BTBT-C8 and the 20:1 blend. (c) Variable temperature PXRD patterns of 20:1 blended powder. The peaks belonging to crystals of C8-BTBT-C8, and C8-BTBT-C8-TCNQ CT crystals are indexed using \* and #, respectively.

## 2. Directional crystallization of C8-BTBT-C8: TCNQ blends in $\nabla T$ .

### 2.1 Crystallization conditions.

The samples were prepared by adopting a sandwiched geometry, that is, depositing 0.5 mg of C8-BTBT-C8:TCNQ blended powder between two glass (or PDMS/glass) substrates (Figure 1). No dewetting occurred for sandwiched films. Uncoated glass and PDMS coated glass were chosen

to investigate the influence of the substrate on crystallization. The molar ratio of C8-BTBT-C8:TCNQ, and the cooling rate were varied to conduct the directional crystal growth of blended samples in  $\nabla T$ , and to explore a broad set of crystallization conditions. For these, the cooling rates at the growth front  $C_{exp}$  were varied from 0.6 to 60 °C min<sup>-1</sup> (films **1-14**, Table S5).

## ***2.2 Growth morphology and thin-film morphology of the blends on the glass substrate.***

The crystal growth processes of samples **1–10** (on pure glass substrates) were monitored in situ by POM during directional crystallization (Figure 3). The digitated growth morphology<sup>27</sup> was observed in films **3, 4, 8, and 9**. On the other hand, films **1, 2, 6, and 7** show branched sea-weed type growth morphology. In addition, films **5 and 10** exhibit dendritic growth morphology. The results indicate that the cooling rate at the growth front  $C_{exp}$  (°C min<sup>-1</sup>) plays a vital role in determining the crystal growth morphology: moderate  $C_{exp}$  (6 and 12°C min<sup>-1</sup>) leads to the digitated growth, but too slow ( $\leq 3^\circ\text{C min}^{-1}$ ) or too fast ( $\geq 60^\circ\text{C min}^{-1}$ )  $C_{exp}$  perturbs the growth (Figure 4). As shown in Figure S17, after the  $\nabla T$  crystallization, the crystalline stripes can be observed again in films **3, 4, 8, and 9**. The width of the larger stripes ranges from 30  $\mu\text{m}$  to 80  $\mu\text{m}$ , and the width of the narrower stripes ranges from 5  $\mu\text{m}$  to 30  $\mu\text{m}$  (Table S6). Only faceted or mosaic crystals were found in other films (**1, 2, 5, 6, 7 and 10**, Figure S17). The thickness values of films, measured by a step profiler, range between 2~3  $\mu\text{m}$ . However, many cracks through the thin films were found after cooling the films from  $T_c$  to room temperature. These originate from the differences in thermal expansion coefficients between organic crystals and the rigid glass substrate. Another problem is that after separating the two glass slides, almost equal amounts of material remained on the top and bottom glass substrates due to the relatively large adhesion of organic crystals to glass. Using PDMS/glass substrates improved these problems (*vide infra*).

To investigate the crystal structures, out-of-plane preferred orientation and in-plane alignment of the thin films, diffraction studies have been conducted on these films with in-house *s*XRD and synchrotron-based GIXD based facilities. Figure S21 shows the *s*XRD patterns of the thin films **1-10**, indicating that the known crystal phase of C8-BTBT-C8 and C8-BTBT-C8-TCNQ CT (Figure S1 and Table S1) that have been detected in the bulk crystals are also present in thin films. No other polymorphs have been detected in the thin films at room temperature. Diffraction data demonstrate a high preferential orientation of the (00 $l$ ) lattice planes parallel to the glass substrates for both C8-BTBT-C8 and C8-BTBT-C8-TCNQ CT crystallites. Synchrotron-based 2D-GIXRD patterns displayed in Figure S24 (for films **3**, **4**, **8** and **9**) exhibit a texture with a low mosaicity. All spots in GIXD data can be indexed by the known crystal phase of C8-BTBT-C8 and C8-BTBT-C8-TCNQ CT.<sup>17, 18</sup> Synchrotron results also corroborates a lack of polymorphism in the thin films and a high preferential orientation of the (00 $l$ ) planes for both crystallites, which are consistent with the observations made by *s*XRD.

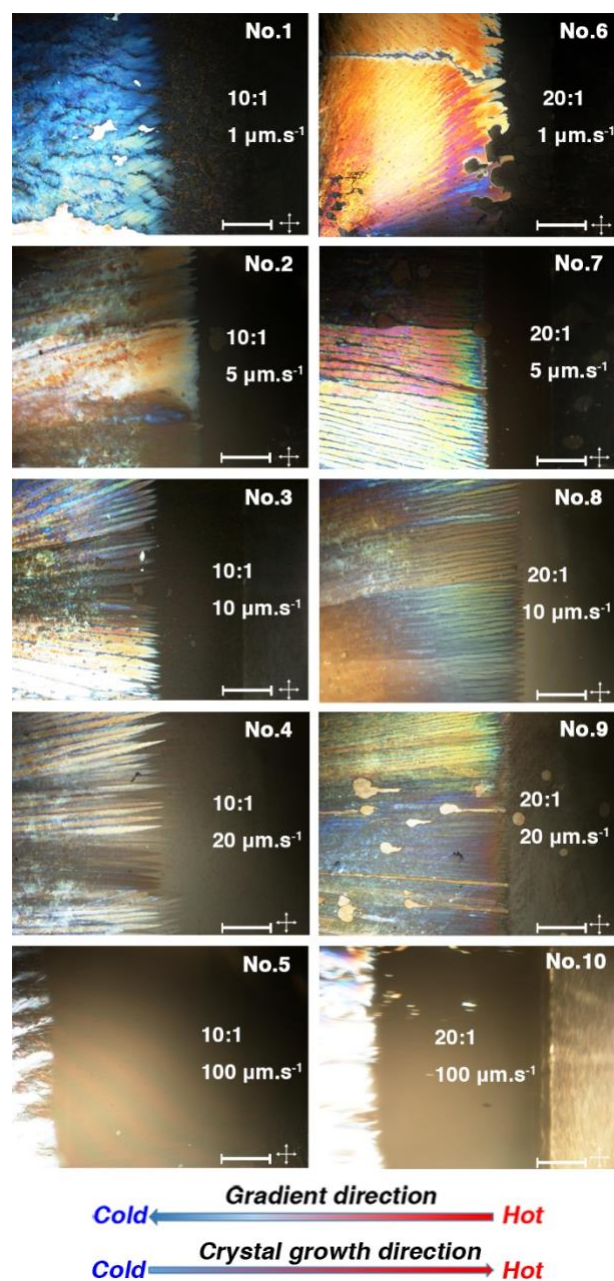


**Figure 3.** The crystal growth front of the blended films **1-10** on glass substrates under different VT crystallization conditions. The scale bar is 500  $\mu\text{m}$ . All the pictures were recorded during the VT experiments under crossed polarizers. The thermal gradient direction and the crystal growth direction are highlighted at the bottom.

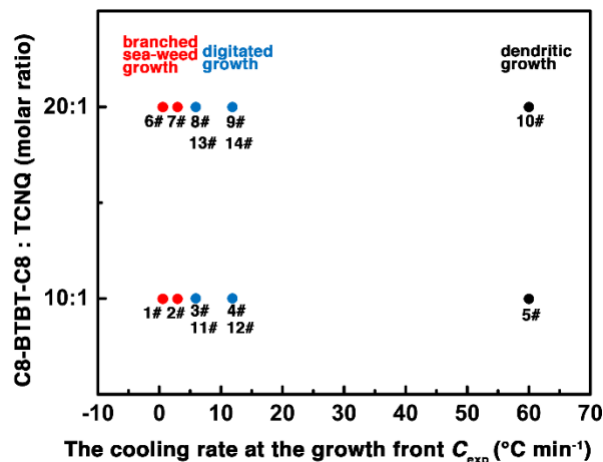


**Figure 4.** A diagram shows the sample zones with branched sea-weed growth, dendritic growth, and dendritic growth morphologies under different crystallization conditions.

### 2.3 Growth morphology and thin-film morphology of the blends on the PDMS/glass substrate.

The formation of cracks is a common problem when preparing organic thin films from melt crystallization. Therefore, a soft PDMS layer was used to coat glass substrates. Figure 5a and Figure S18 show that films **11-14** on the PDMS/glass substrate keep a digitated growth front during the  $\nabla T$  crystallizations. As expected, after directional crystallization, fewer cracks are present (Figure 5b and Figure S19) in the samples compared to the samples prepared on pure glass substrates, resulting from the soft viscoelastic nature of PDMS. The comparison of the dark-field microscopy picture of film **9** (on the glass substrate) with film **14** (on the PDMS/glass substrate) also indicates that the soft PDMS layer can improve the cracking problem (Figure S20). Samples of 20:1 ratio (films **13** and **14**) show better parallel striped crystals than 10:1 ratio samples (films **11** and **12**). The widths of crystallite stripes in films **13-14** correspond to the values of the thin films obtained on glass substrates (Table S6).

The morphology of stripes for sample **14** was further analyzed using confocal Raman imaging. First, Raman spectra of pure TCNQ and C8-BTBT-C8 materials were measured (Figure S21). For

mapping the spatial distribution of TCNQ molecules, the following vibrational modes at  $1212\text{ cm}^{-1}$ ,  $1460\text{ cm}^{-1}$  and  $1607\text{ cm}^{-1}$  can be used, which belong to C=CH bending, C-CN stretching and C=C ring stretching, respectively<sup>28</sup>. However, the first two overlap with the C8-BTBT-C8 vibrational modes at  $1208\text{ cm}^{-1}$  and  $1472\text{ cm}^{-1}$ , while only the vibrational mode at  $1607\text{ cm}^{-1}$  has no overlap with any of the C8-BTBT-C8 vibrational modes<sup>29,30</sup>. For this reason, the peak intensity at  $1607\text{ cm}^{-1}$  was used to map the spatial distribution of TCNQ shown in Figure 6a. The well-defined horizontal stripes indicate regions of increased TCNQ concentration in agreement with the POM images (Figure 5). In addition, the numerically integrated vertical line scans across the entire Raman map are shown in Figure 6b. The graph reveals that the concentration contrast between the TCNQ-rich and TCNQ-depleted regions is at a level of some 50%.

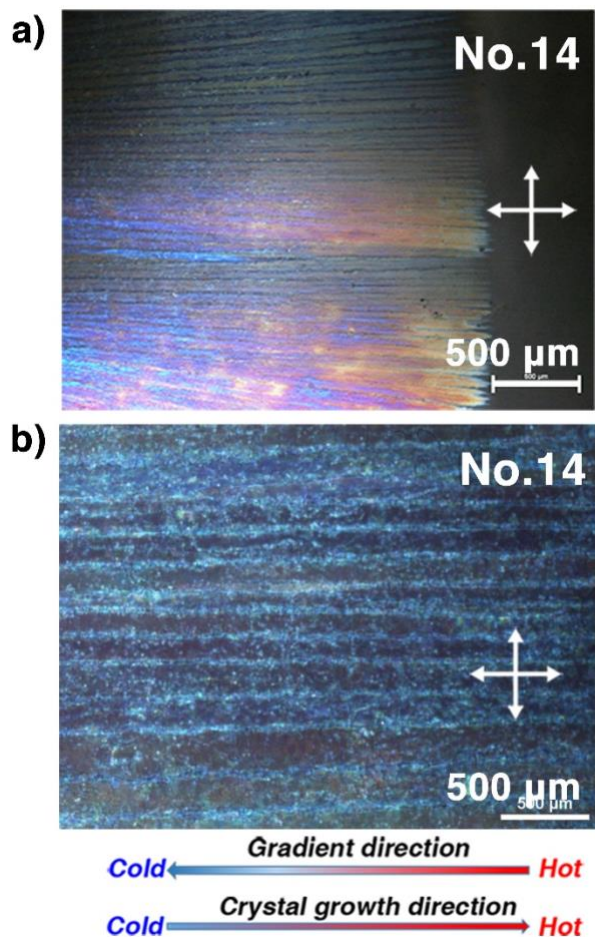


**Figure 5.** POM images of film 14 prepared on PDMS coated glass with a molar ratio 20:1, a withdrawal speed of  $20 \mu\text{m}\cdot\text{s}^{-1}$  during (a) and after (b) the  $\nabla T$  crystallization process. The gradient and crystal growth directions are given at the bottom.

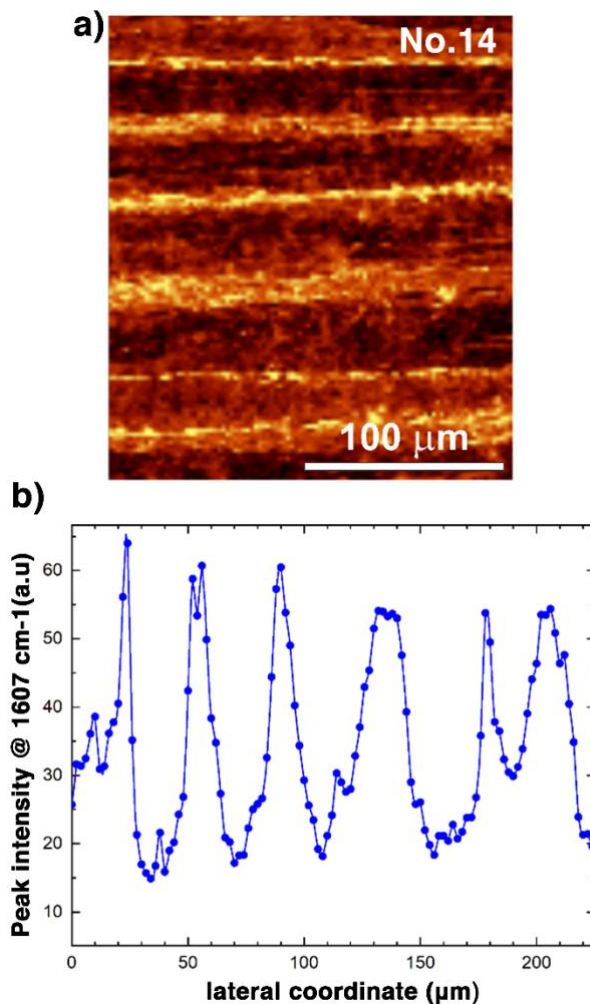


**Figure 6.** Confocal Raman mapping. a) Distribution map of the TCNQ Raman signal at  $1607 \text{ cm}^{-1}$ . b) Spatial modulation of the TCNQ Raman signal obtained by numerical integration of vertical line scans of the entire Raman map.

Like films prepared on glass substrates, the single observation of the  $00l$  family of C8-BTBT-C8 and C8-BTBT-C8-TCNQ CT diffraction spots through the whole specular diffraction pattern for films **11-14** (Figure 7 and Figure S23) demonstrates a high preferential orientation of the  $(00l)$

planes parallel to the PDMS layer. Again, only the known crystal phases C8-BTBT-C8 and C8-BTBT-C8-TCNQ CT can be observed in the XRD patterns of films **11-14**. Moreover, the synchrotron-based GIXD diffraction patterns are shown in Figure 8 (for film **14**) and Figure S25 (for film **11-14**). The GIXD data agree well with the *s*XRD results of films **11-14**, highlighting a lack of polymorphism and the high preferential orientation of the (00*l*) plane family for both C8-BTBT-C8 and C8-BTBT-C8-TCNQ CT crystallites.

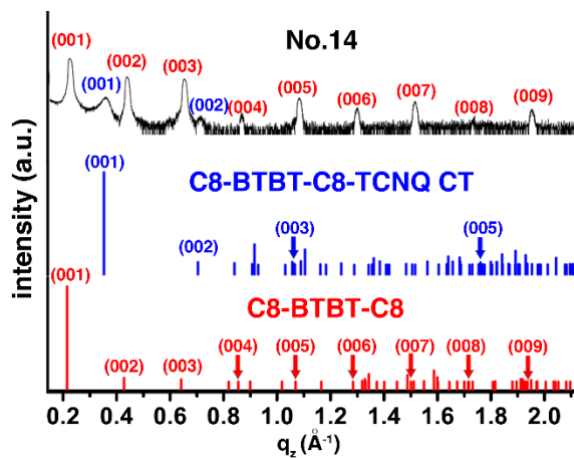


**Figure 7.** Specular X-ray diffraction patterns of film **14** together with calculated diffraction pattern for randomly oriented crystallites.



molecules in film **14** were well in-plane aligned along the [010] or [0-10] direction, which is parallel to the gradient direction of the  $\nabla T$  approach (Figure 10a). This result agrees well with the POM images shown in Figure 5a and 5b. It should be noted that processing pure C8-BTBT-C8 films by directional crystallization leads to no uniaxial alignment.<sup>20</sup> The absence of uniaxial alignment has also been observed for C8-BTBT-C8-TCNQ CT in Figure 9b. Pole figures of films **3**, **4**, **8** and **9** (glass substrates) and films **11-14** (PDMS/glass substrates) are shown in Figure **S26a** and Figure **S26b**, respectively. These results corroborate those of film **14**, except that some discrete {113} reflections are missing, most likely due to weak signal intensity. In summary, both C8-BTBT-C8 and C8-BTBT-C8-TCNQ CT crystallites show a high preferential orientation of the (00 $l$ ) planes, which means that C8-BTBT-C8 molecules and C8-BTBT-C8-TCNQ CT molecules preferentially stand upright on the glass substrate or on the PDMS/glass substrate (Figure 10b and Figure S27).

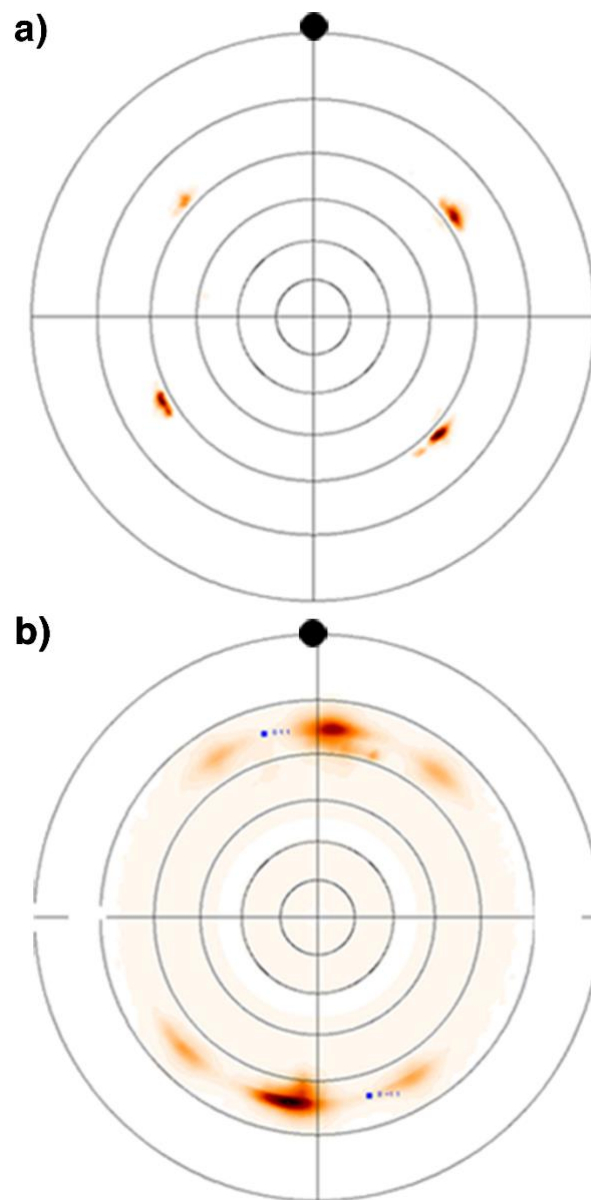


**Figure 9.** (a) Pole figure of the  $\{113\}$  reflection of C8-BTBT-C8 crystallites, and (b) of the  $\{01-1\}$  reflection of C8-BTBT-C8-TCNQ CT crystallites of film **14**. The pole figures were calculated based on the rotating GIXD measurements. The solid black dots highlight the thermal gradient direction.

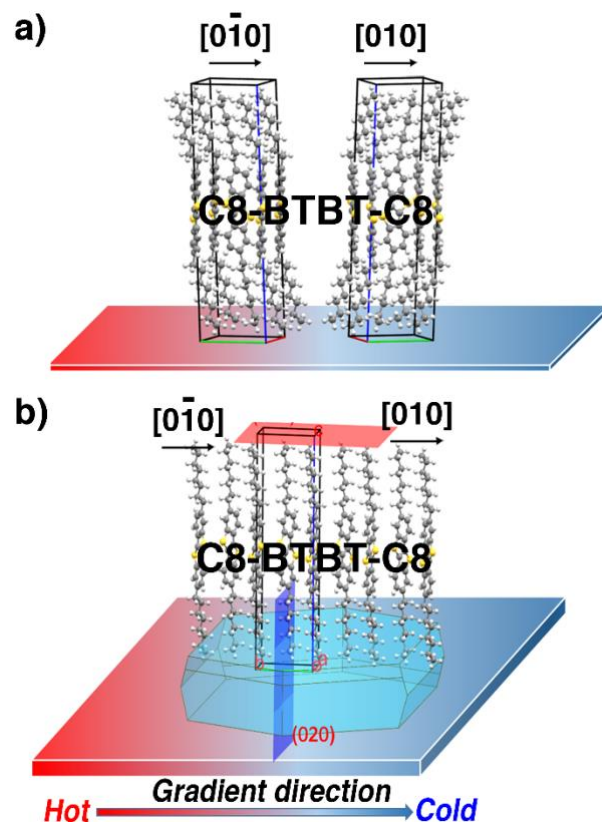


**Figure 10.** (a) Schematic representation of C8-BTBT-C8 molecular orientation versus the substrate (glass or PDMS/glass), and (b) the two possible in-plane alignment direction of C8-BTBT-C8 unit cells in the samples. The  $\nabla T$  direction is highlighted at the bottom.

## CONCLUSIONS

The directional crystal growth of semiconductors has been demonstrated so that separated areas of p- and n-type semiconductors are formed. Variable temperature powder XRD patterns (PXRD), differential scanning calorimetry (DSC) and polarized optical microscopy (POM) results show that 10:1 and 20:1 molar ratios of C8-BTBT-C8:TCNQ blends exhibit a phase behavior rather comparable to pure C8-BTBT-C8, qualifying them for directional crystallization. The results indicate that the crystal growing modes (digitated, dendritic, or branched sea-weed type) of the

blends are linked to the cooling speed, which is externally imposed by the lateral withdrawal velocity and the magnitude of the thermal gradient. On both glass and PDMS substrates, the parallel crystalline stripes of C8-BTBT-C8 and C8-BTBT-C8-TCNQ CT have been obtained at a moderate cooling rate (6 or 12°C min<sup>-1</sup>), and a clear assignment of the different stripes to the different crystalline phases are obtained by Raman microscopy. The comprehensive characterization of the structure and the morphology of blend thin films was completed by POM, in-house XRD and synchrotron-based GIXD measurements. The results confirm a preferential orientation of the crystallites with the (001) plane parallel to the substrate surface for both types of phases. Moreover, the in-plane alignment of both phase types along the thermal gradient direction has been confirmed. While C8-BTBT-C8 shows high crystalline alignment with low in-plane mosaicity, the order is less pronounced for the charge transfer complex C8-BTBT-C8-TCNQ CT.

## ASSOCIATED CONTENT

### **Supporting Information.**

The Supporting Information is available free of charge on the ACS Publications website at DOI: XXX, including the crystal structure information, calibration of the magnitude of the temperature gradient set-up, TGA and DSC curves, variable temperature PXRD patterns, optical microscopy images, Raman spectra, in-house *s*XRD patterns, synchrotron-based GIXD and Pole-figures.

Corresponding Author

\* guangfeng.liu@ulb.be

## **ORCID**

Guangfeng Liu: 0000-0001-5029-3794

Jie Liu: 0000-0002-1301-057X.

Andrew Dunn: 0000-0002-8417-8468

Peter Nadazdy: 0000-0001-7354-949X

Peter Siffalovic: 0000-0002-9807-0810

Roland Resel: 0000-0003-0079-3525

Mamatimin Abbas: 0000-0003-0222-5994

Guillaume Wantz: 0000-0002-3031-3687

Yves Geerts: 0000-0002-2660-5767

## **Note**

The authors declare no competing financial interest.

## **ACKNOWLEDGMENT**

G.L. thanks the European Union's Horizon 2020 Research and Innovation Program under the Marie Skłodowska-Curie grant agreement n°. 791207 (PARADA) and postdoctoral fellowship support from the FNRS for the POLYMOL project n° 1.B.253.20F. YG is thankful to the Belgian National Fund for Scientific Research (FNRS) for financial support through research projects

BTBT n° 2.4565.11, Phasetrans n° T.0058.14, Pi-Fast n° T.0072.18, and 2D to 3D No. 30489208. Financial supports from the French Community of Belgian (ARC n° 20061) and by the Walloon Region (WCS No. 1117306, SOLIDYE n° 1510602) are also acknowledged. We thank the synchrotron Elettra, Trieste for provision of synchrotron radiation and Luisa Barba for her support to use the beamline XRD1.

## REFERENCES

- (1) Shirakawa, H.; Louis, E. J.; MacDiarmid, A. G.; Chiang, C. K.; Heeger, A. J., Synthesis of electrically conducting organic polymers: halogen derivatives of polyacetylene, (CH). *J. Chem. Soc., Chem. Commun.*, **1977**, *16*, 578-580.
- (2) Yamamoto, Y.; Yoshino, K.; Inuishi, Y., Electrical Properties of Phthalocyanine-Halogen Complexes. *J. Phys. Soc. Jpn.*, **1979**, *47* (6), 1887-1891.
- (3) Jacobs, I. E.; Moulé, A. J., Controlling Molecular Doping in Organic Semiconductors. *Adv Mater.* **2017**, *29* (42), 1703063.
- (4) Lüssem, B.; Keum, C.-M.; Kasemann, D.; Naab, B.; Bao, Z.; Leo, K., Doped Organic Transistors. *Chem Rev.* **2016**, *116* (22), 13714-13751.
- (5) Salzmann, I.; Heimel, G.; Oehzelt, M.; Winkler, S.; Koch, N., Molecular Electrical Doping of Organic Semiconductors: Fundamental Mechanisms and Emerging Dopant Design Rules. *Acc Chem Res.* **2016**, *49* (3), 370-378.
- (6) Schweicher, G.; Garbay, G.; Jouclas, R.; Vibert, F.; Devaux, F.; Geerts, Y. H., Molecular Semiconductors for Logic Operations: Dead-End or Bright Future? *Adv Mater.* **2020**, *32* (10), 1905909.

- (7) Ohashi, C.; Izawa, S.; Shinmura, Y.; Kikuchi, M.; Watase, S.; Izaki, M.; Naito, H.; Hiramoto, M., Hall Effect in Bulk-Doped Organic Single Crystals. *Adv Mater.* **2017**, *29* (23), 1605619.
- (8) Mullins, W. W.; Sekerka, R. F., Morphological Stability of a Particle Growing by Diffusion or Heat Flow. *J. Appl. Phys.* **1963**, *34* (2), 323-329.
- (9) Mullins, W. W.; Sekerka, R. F., Stability of a Planar Interface During Solidification of a Dilute Binary Alloy. *J. Appl. Phys.* **1964**, *35* (2), 444-451.
- (10) Jackson, K. A.; Hunt, J. D., Transparent compounds that freeze like metals. *Acta Met.* **1965**, *13* (11), 1212-1215.
- (11) Langer, J. S., Instabilities and pattern formation in crystal growth. *Rev. Mod. Phys.* **1980**, *52* (1), 1-28.
- (12) Caroli, B.; Caroli, C.; Roulet, B., The Mullins-Sekerka instability in directional solidification of thin samples. *J. Crystal Growth.* **1986**, *76* (1), 31-49.
- (13) Godreche, C., Solids far from equilibrium. Cambridge University Press, **2011**
- (14) Akamatsu, S.; Faivre, G.; Ihle, T., Symmetry-broken double fingers and seaweed patterns in thin-film directional solidification of a nonfaceted cubic crystal. *Phys. Rev. E* **1995**, *51* (5), 4751-4773.
- (15) Ginibre, M.; Akamatsu, S.; Faivre, G., Experimental determination of the stability diagram of a lamellar eutectic growth front. *Phys. Rev. E* **1997**, *56* (1), 780-796.
- (16) Shibata, Y.; Tsutsumi, J. y.; Matsuoka, S.; Matsubara, K.; Yoshida, Y.; Chikamatsu, M.; Hasegawa, T., Uniaxially oriented polycrystalline thin films and air-stable n-type transistors based on donor-acceptor semiconductor (diC8BTBT)(FnTCNQ) [n = 0, 2, 4]. *Appl. Phys. Lett.* **2015**, *106* (14), 143303.

- (17) Tsutsumi, J.; Matsuoka, S.; Inoue, S.; Minemawari, H.; Yamada, T.; and Hasegawa, T., N-type field-effect transistors based on layered crystalline donor-acceptor semiconductors with dialkylated benzothienobenzothiophenes as electron donors. *J. Mater. Chem. C*, **2015**, *3*, 1976-1981.
- (18) Ebata, H.; Izawa, T.; Miyazaki, E.; Takimiya, K.; Ikeda, M.; Kuwabara, H.; Yui, T., Highly Soluble [1]Benzothieno[3,2-*b*]benzothiophene (BTBT) Derivatives for High-Performance, Solution-Processed Organic Field-Effect Transistors. *J. Am. Chem. Soc.* **2007**, *129* (51), 15732-15733.
- (19) Ruzié, C.; Karpinska, J.; Laurent, A.; Sanguinet, L.; Hunter, S.; Anthopoulos, T. D.; Lemaur, V.; Cornil, J.; Kennedy, A. R.; Fenwick, O.; *et al.*, Design, synthesis, chemical stability, packing, cyclic voltammetry, ionisation potential, and charge transport of [1]benzothieno[3,2-*b*][1]benzothiophene derivatives. *J. Mater. Chem. C* **2016**, *4* (22), 4863-4879.
- (20) Schweicher, G.; Liu, G.; Fastré, P.; Resel, R.; Abbas, M.; Wantz, G.; Geerts, Y. H., Directional crystallization of C8-BTBT-C8 thin films in a temperature gradient. *Mater. Chem. Front.* **2021**, *5* (1), 249-258.
- (21) Netzsch Proteus Software Available online: <https://www.netzsch-thermal-analysis.com/en/products-solutions/software/proteus/>
- (22) A. Bravais, *Etudes Cristallographiques*. Gauthier-Villars: **1866**.
- (23) G. Friede, Crystal Morphologies, *Bull. Soc. Franc. Mineral.* **1907**, *30*, 326-455.
- (24) J. D. H. Donnay and D. Harker, A new law of crystal morphology extending the law of Bravais, *Am. Mineral.* **1937**, *22*, 446-467.

- (25) Schrode, B.; Pachmajer, S.; Dohr, M.; Rothel, C.; Domke, J.; Fritz, T.; Resel, R.; Werzer, O., GIDVis: a comprehensive software tool for geometry-independent grazing-incidence X-ray diffraction data analysis and pole-figure calculations. *J. Appl. Crystallogr.* **2019**, *52* (3), 683-689.
- (26) I. Salzmann, R. Resel, software for the analysis of X-ray diffraction pole figures with IDL, *J. Appl. Crystallogr.* **2004**, *37*, 1029-1033.
- (27) K. A. Jackson, *Kinetic Processes: Crystal Growth, Diffusion, and Phase Transitions in Materials.*, Wiley: **2010**.
- (28) Gucciardi, P. G.; Trusso, S.; Vasi, C.; Patanè, S.; Allegrini, M., Nano-Raman imaging of Cu–TCNQ clusters in TCNQ thin films by scanning near-field optical microscopy. *Phys. Chem. Chem. Phys.* **2002**, *4* (12), 2747-2753.
- (29) Mai, J.; Tang, N.; He, W.; Zou, Z.; Luo, C.; Zhang, A.; Fan, Z.; Wu, S.; Zeng, M.; Gao, J.; *et al.*, Effects of Ambient Gases on the Electrical Performance of Solution-Processed C8-BTBT Thin-Film Transistors. *Nanoscale Res. Lett.* **2019**, *14* (1), 169.
- (30) Li, Y.; Liu, C.; Lee, M. V.; Xu, Y.; Wang, X.; Shi, Y.; Tsukagoshi, K., In situ purification to eliminate the influence of impurities in solution-processed organic crystals for transistor arrays. *J. Mater. Chem. C.* **2013**, *1* (7), 1352-1358.

### For Table of Contents Only:

